An analysis of dislocation nucleation near a free surface

Liu, Yufu; Van der Giessen, Erik; Needleman, Alan

Published in:
International Journal of Solids and Structures

DOI:
10.1016/j.ijsolstr.2006.07.017

Publication date:
2007

Available online at www.sciencedirect.com
ScienceDirect
International Journal of Solids and Structures 44 (2007) 1719–1732
INTERNATIONAL JOURNAL OF SOLIDS and STRUCTURES
www.elsevier.com/locate/ijsolstr

An analysis of dislocation nucleation near a free surface

Yufu Liu [a], Erik Van der Giessen [b,*], Alan Needleman [c]

[a] *Research Center for Advanced Science and Technology, The University of Tokyo, 4-6-1 Komaba, Meguro, Tokyo 153-8904, Japan*
[b] *Department of Applied Physics, Materials Science Center, University of Groningen, Nyenborgh 4, 9747 AG Groningen, The Netherlands*
[c] *Division of Engineering, Brown University Providence, RI 02912, USA*

Received 20 April 2006
Available online 28 July 2006

Guest Editor: Guruswami Ravichandran

Abstract

Molecular dynamics analyses of defect-free aluminum single crystals subject to bending are carried out to investigate dislocation nucleation from free surfaces. A principal aim of the analyses is to provide background for the development of dislocation nucleation criteria for use in discrete dislocation plasticity calculations. The molecular dynamics simulations use an embedded atom potential for aluminum. Bending is imposed on a strip by specifying a linear variation of displacement rate on opposite edges. The overall bending response is determined and the character of the dislocations nucleated is identified. It is found that the stress magnitudes at the instant of dislocation nucleation are nearly an order of magnitude smaller than for homogeneous bulk dislocation nucleation. The characterization of dislocation nucleation in terms of various phenomenological nucleation criteria is explored, in particular: (i) a critical resolved shear stress; (ii) the onset of an elastic instability; and (iii) a critical stress-gradient criterion. It is found that dislocation nucleation is not well-represented by a critical value of the resolved shear stress but is reasonably well-represented by the critical stress-gradient criterion.

Keywords: Dislocation nucleation; Free surface; Plasticity; Size effect; Molecular dynamics; Pure bending

1. Introduction

Theories of dislocation nucleation have focused on nucleation from internal defects, in particular from Frank-Read sources (e.g., Kubin and Canova, 1992; Van der Giessen and Needleman, 1995; Zbib et al., 1998; Benzerga et al., 2004) and from crack tips (e.g., Rice and Thomson, 1974; Beltz and Rice, 1992; Xu et al., 1995). When the deformed volume is small, the number of internal defects is small and, in fact, internal defects may be absent so that the possibilities for dislocation nucleation are either homogeneous nucleation in the bulk or from surfaces. Homogeneous dislocation nucleation in defect-free bulk crystals subject to indentation has been studied both experimentally and theoretically (e.g., Kelchner et al., 1998; Shenoy et al., 2000;

* Corresponding author. Tel.: +31 50 363 8046; fax: +31 50 363 4886.
E-mail address: e.van.der.giessen@rug.nl (E. Van der Giessen).

0020-7683/$ - see front matter © 2006 Elsevier Ltd. All rights reserved.
doi:10.1016/j.ijsolstr.2006.07.017

Li et al., 2002; Christiansen et al., 2002). Depending on the geometry of the indenter and the morphology of the crystal surface, the first dislocation may be nucleated in the interior (Shenoy et al., 2000; Li et al., 2002) or from the free surface (Kelchner et al., 1998; Christiansen et al., 2002). The studies of Shenoy et al. (2000) and of Miller and Acharya (2004) showed that homogeneous nucleation in the bulk is not governed by a critical value of the maximum resolved shear stress and alternative criteria were proposed.

The atomic environment at a free surface is, of course, different from that in the bulk and one motivation of our work is to explore the implications of this difference for dislocation nucleation. The issue of dislocation nucleation from surfaces is also of direct relevance in a variety of applications. For example, control of surface morphology during processing of thin films is key and dislocation nucleation at a free surfaces affects the surface morphology that develops. Also, micro/nano–electro-mechanical systems (MEMS/NEMS) have large surface to volume ratios so that surfaces are a potential source of defects that limit the performance and reliability of these systems.

Several atomistic analyses of dislocation nucleation from surfaces have been carried out, e.g., Brochard et al. (2001), Shan et al. (2005) and Weingarten and Selinger (2006). Here, the focus is on exploring the extent to which dislocation nucleation from a free surface can be characterized by a phenomenological nucleation criterion that can be used in a discrete dislocation plasticity framework. The specific problem analyzed is bending of a single crystal strip. Classical molecular dynamics calculations are carried out using the embedded atom method (Daw and Baskes, 1984) with the Ercolessi and Adams (1994) potential for aluminum. The strip has a rectangular cross-section in the plane of deformation while out-of-plane periodic boundary conditions are imposed so that the depth of the strip is effectively infinite. Loading is imposed through prescribed displacements that correspond to a pure rotation of the sides of the strip. Within the context of linear elasticity and with a suitably oriented crystal, this corresponds to pure bending, with equal magnitude tensile and compressive stresses about the centerline. However, when the strains are large enough for nonlinear elastic effects to come into play, the symmetry of the stress state about the centerline is broken. Nevertheless, the largest magnitude deformation still occurs at the free surfaces, thus promoting defect nucleation there. In addition, bending or combined bending and axial deformation is a common mode of deformation in structures so that the deformation state analyzed here is of direct relevance for MEMS/NEMS devices.

In discrete dislocation plasticity, the long-range interactions between dislocations is accounted for by their elastic fields while constitutive rules are used to govern other aspects, in particular dislocation nucleation. No general constitutive rule is currently available for dislocation nucleation from a free surface although progress is being made, Gao et al. (submitted for publication) and Yu et al. (accepted for publication). An aim of our analyses is to provide background for the development of criteria for dislocation nucleation that can be used in discrete dislocation plasticity analyses (e.g., Kubin and Canova, 1992; Van der Giessen and Needleman, 1995; Zbib et al., 1998; Benzerga et al., 2004).

2. Model and computational procedure

Classical molecular dynamics simulations are carried out using the embedded atom method (EAM) potential of Ercolessi and Adams (1994). This potential was based on fitting various property values obtained from *ab initio* calculations, for example, elastic moduli, the equilibrium lattice spacing and the cohesive energy. However, some properties such as the intrinsic (1 1 1) stacking fault energy and the relaxed surface configurations for the (1 1 1), (1 0 0) and (1 1 0) surfaces are not represented accurately.

The configuration analyzed is illustrated in Fig. 1(a). A single fcc crystal is oriented such that the plane of the figure is the (1 1 1) plane. The x_1-direction is identified with the $\pm[\bar{1}\,0\,1]$ direction, the x_2-direction is identified with the $[1\,\bar{2}\,1]$ direction and the out-of-plane x_3-direction is [1 1 1]. The in-plane dimensions of the crystal are $L_1 \times L_2$. Calculations are carried out for three crystal sizes: (I) $L_1 = 100d_1$, $L_2 = 20d_2$; (II) $L_1 = 120d_1$, $L_2 = 30d_2$; and (III) $L_1 = 170d_1$, $L_2 = 50d_2$. Here, $d_1 = a/\sqrt{2}$ and $d_2 = \sqrt{3/2}a$ (Fig. 1(b)), with $a = 0.4032$ nm being the lattice parameter of pure aluminum at 0 K. Hence, crystal I is 28.51 nm × 9.87 nm; crystal II is 34.21 nm × 14.81 nm; and crystal III is 48.47 nm × 24.69 nm. In all cases, the out-of-plane dimension is $L_3 = 2d_3 = a\sqrt{12} = 1.39$ nm. The number of atoms is 24,282 in crystal I, 43,562 in crystal II and 102,542 in crystal III. Atoms located within $L_1/2 - L_0 \leqslant x \leqslant L_1/2$ and $-L_1/2 \leqslant x \leqslant -L_1/2 + L_0$ (the shaded

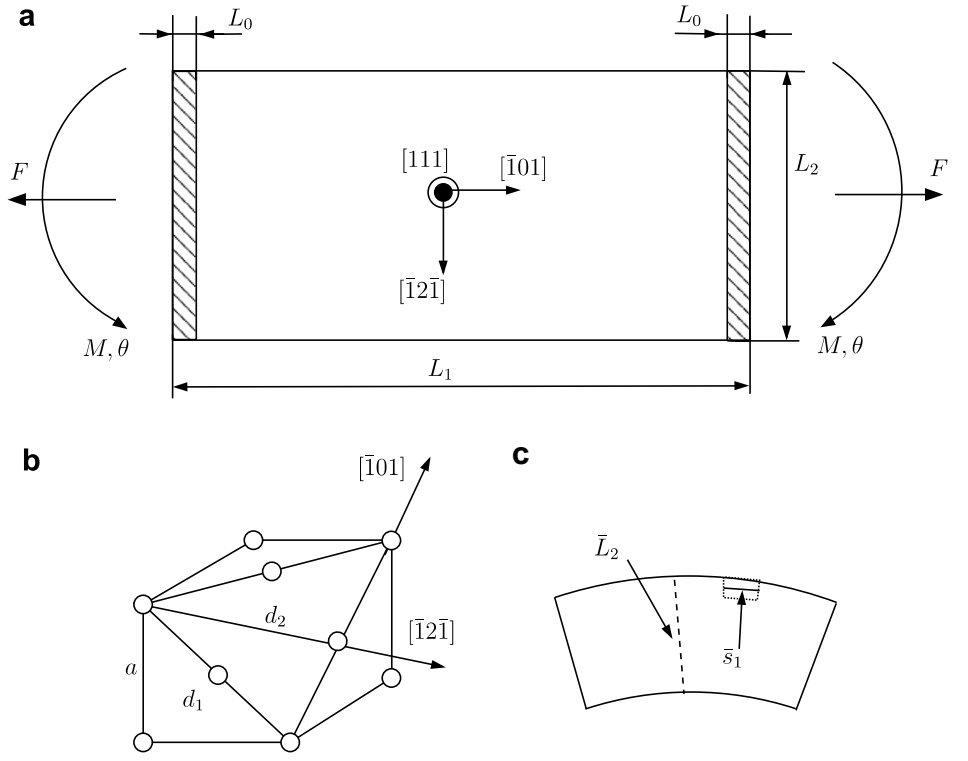

Fig. 1. (a) Schematic of bending model geometry and crystal orientation. Crystal directions of $[\bar{1}\,0\,1]$, $[1\,\bar{2}\,1]$ and $[1\,1\,1]$ are referred to as x_1, x_2 and x_3 coordinate axes in the text, respectively. The origin of the (x_1, x_2)-coordinate system is assumed to be at the center of the model. θ and M are bending angle and moment, respectively, as detailed in the text; F is the average axial force generated by the boundary conditions. (b) Schematic showing the geometry of d_1 and d_2. (c) Schematic bending deformation. Two surface atoms initially parallel to the x_2-axis and a distance L_2 apart are bent to $\bar{L}_2$ which is used later in Eq. (4). $\bar{s}_1$ is the width of the mid-section of the volume over which stress and strain are calculated in the current configuration.

regions in Fig. 1) are designated as boundary atoms and are constrained by the imposed boundary conditions. The positions of the remaining active atoms are determined from the molecular dynamics calculations.

The boundary atoms are subject to a displacement rate that varies linearly with x_2

$$\dot{u}_1 = \pm\dot{\theta}x_2 \tag{1}$$

where u_1 denotes the displacement of an atom in the x_1-direction, $\dot{(\,)}$ denotes $\partial(\,)/\partial t$ and θ is the prescribed rotation. In (1), the positive sign applies for the boundary atoms near $x_1 = L_1/2$ and the negative sign for the boundary atoms near $x_1 = -L_1/2$. The motion of the boundary atoms in the x_2- and x_3-directions is unconstrained except for the requirement so that the length L_3 is fixed. The value of L_0 (see Fig. 1a) was taken to be $2.5d_1$; numerical experiments showed that smaller values of L_0 led to decohesion along the interface between the boundary and active atoms.

Isothermal calculations are carried out with the temperature taken to be near absolute zero, 10^{-3} K. The initial velocities of the atoms are generated using a Boltzmann distribution at the specified temperature. Then, the positions of the boundary atoms were fixed near their perfect lattice sites and their x_1-velocities were set to zero. In some of the calculations, the active atoms were allowed to relax in order to reduce the energy at the free surfaces $x_2 = \pm L_2$ prior to imposing any loading.

The calculations are carried out using a fixed time step of $\Delta t = 3 \times 10^{-3}$ ps. In the first time step, the boundary atoms are subject to a rotation rate of $\dot{\theta} = 2 \times 10^{-7}/\Delta t = 6.67 \times 10^{7}$ s^{-1}. Then, with the positions of the boundary atoms fixed 5000 time steps are taken to permit the active atoms to find a relaxed configuration. In the next time step, the boundary atoms are again subject to a rotation rate of $\dot{\theta} = 2 \times 10^{-7}/\Delta t$ followed by

5000 times steps with the boundary atom positions fixed. This time stepping procedure is repeated until the calculation is terminated.

As deformation proceeds, the volume of the system changes slightly due to surface relaxation and the external loading. Some test cases using both the Nose (1984) and Hoover (1985) thermostat and a velocity scaling algorithm (cf. Allen and Tildesley, 1987) were implemented to keep the temperature constant. The Nose–Hoover scheme applies a damping factor to the system based on the difference between the current temperature and the desired one, while the scaling algorithm scales atomic velocities uniformly by a factor determined from the difference between the actual temperature and the desired temperature. The two schemes may use slightly different methods to correlate simulation data with macroscopic quantities, i.e., time averages for the scaling algorithm and ensemble averages for the Nose–Hoover thermostat. No significant differences in macroscopic quantities computed using the two approaches were found. Only results obtained using the scaling algorithm (scaled at every time step) are reported subsequently.

The Cauchy stress tensor associated with a volume V is computed as (cf. e.g., Allen and Tildesley, 1987)

$$\boldsymbol{\sigma} = \frac{1}{V}\sum_{\alpha}\{\mathbf{x}^{(\alpha)} \otimes \mathbf{f}^{(\alpha)} + m\mathbf{v}^{(\alpha)} \otimes \mathbf{v}^{(\alpha)}\}, \tag{2}$$

where V is the volume, $\mathbf{x}^{(\alpha)}$ is the position vector of atom α, $\mathbf{f}^{(\alpha)}$ is the force vector acting on atom α calculated from the atomic potential, m is the atom mass, and $\mathbf{v}^{(\alpha)}$ is the velocity vector. The summation is over all the atoms in V.

The imposed loading gives rise to combined bending and axial stress. The resulting bending moment and axial force are calculated from the stress state obtained from (2). Two surface atoms initially parallel to the x_2-axis and a distance L_2 apart are used to define a line in the current configuration. The stress is then calculated over a volume that is of width $4.5d_1$ perpendicular to this plane and of thickness L_3. This volume is divided into sub-volumes of dimension $4.5d_1 \times 2d_2 \times L_3$ and the stress components in each sub-volume are calculated using Eq. (2). The normal stress component σ_{nn} in the direction of the line between the two chosen atoms is calculated by a coordinate transformation. The average of this stress component through the thickness is obtained via

$$\bar{\sigma}_{nn} = \frac{1}{L_3}\int_0^{L_3} \sigma_{nn}\,\mathrm{d}x_3 \tag{3}$$

and axial force F and bending moment M are subsequently computed as

$$F = L_3\int_{-\overline{L}_2/2}^{\overline{L}_2/2} \bar{\sigma}_{nn}\,\mathrm{d}\xi, \quad M = L_3\int_{-\overline{L}_2/2}^{\overline{L}_2/2} \bar{\sigma}_{nn}\xi\,\mathrm{d}\xi \tag{4}$$

where ξ denotes the coordinate tangent to the specified plane with $\xi = 0$ at the center of the crystal. $\overline{L}_2$ is defined in Fig. 1(c) as the radial length of the specimen in the bent configuration.

Even though the deformation behavior exhibits some nonlinearity prior to dislocation nucleation, the deformed centerline and the top and bottom surfaces of the crystal are circular to a very good degree of approximation (within 1% with regard to the radii) except near the edges where the active atoms interface with the boundary atoms. Also, the moment calculation was carried out for sections at two locations along the axis and the obtained values were within 2.0%.

3. Numerical results

3.1. Overall response

Fig. 2 shows the evolution of the bending moment and axial force for the smallest and largest specimens, crystal I and crystal III, respectively. For comparison purposes, the moment is normalized by a reference moment M_0 that is linearly proportional to the rotation as in linear elasticity. For pure bending in linear elasticity the axial force vanishes and the moment-rotation relation is linear. For very small bending angles, the computed moment-rotation relation is linear and the axial force is nearly zero. Deviation from linear elastic

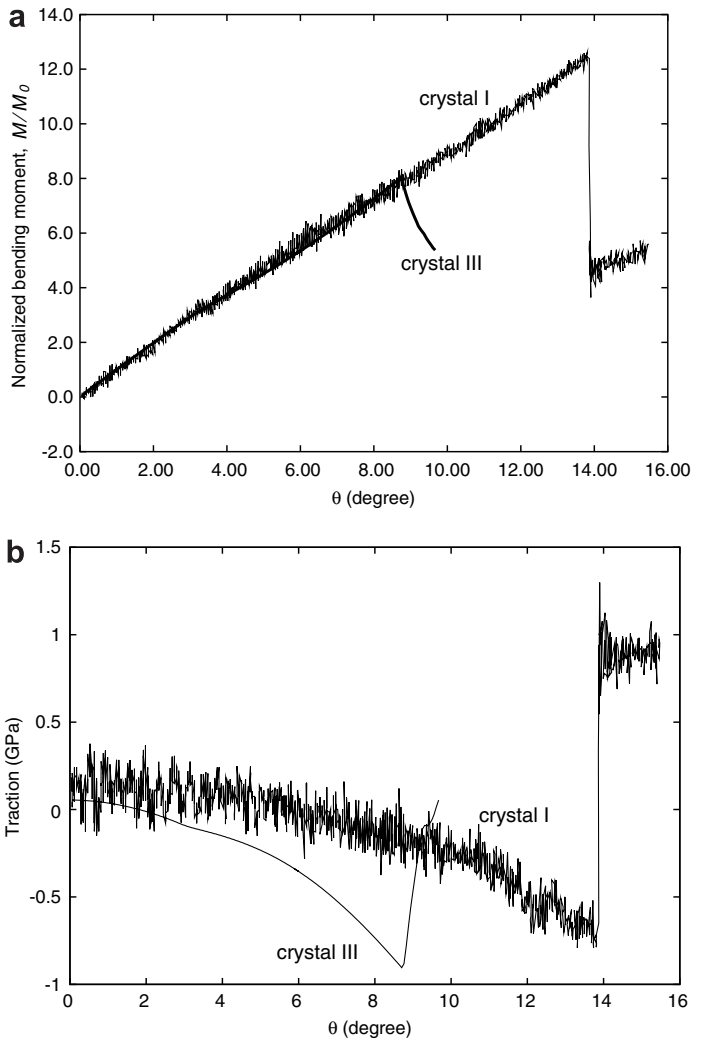

Fig. 2. (a) Normalized bending moment versus bending angle for crystal I and crystal III. (b) Axial traction defined as the axial force F over the cross-sectional area $\bar{L}_2 \times L_3$ versus bending angle for crystal I and crystal III.

behavior occurs at $\theta \approx 1°$ for crystal I and at $\theta \approx 3.5°$ for crystal III. The abrupt change in bending moment and axial force in Fig. 2 is associated with the onset of dislocation nucleation. This occurs at $\theta = 13.8°$ for crystal I and at $\theta = 8.75°$ for crystal III. For crystal II dislocation nucleation occurs at $\theta = 10.31°$.

In all computations here, dislocation nucleation took place at the free surface on the compressive side of the specimen ($x_2 = -L_2/2$). This is, of course, not surprising because of the significant compressive axial force that develops prior to dislocation nucleation. The evolution of the thickness averaged axial stress $\bar{\sigma}_{nn}$ in $4.5d_1 \times 2d_2 \times L_3$ volumes next to the free surfaces for crystal I is shown in Fig. 3. The stress values are calculated in the same slice as used to calculate the bending moment and axial force in Fig. 2. The fluctuations arise from the atomic rearrangements that takes place in the time between increments of imposed rotation. After the stress drops, the system was allowed to relax for 5000 time steps before the next incremental loading was imposed.

The stress magnitude is about a factor of two greater on the compressive side than on the tensile side, consistent with a compressive axial force. When dislocation nucleation initiates, the stress magnitude decreases on both the compressive and tensile sides. The shear stress $\sigma_{n\xi}$ as well as the orthogonal normal stress (not shown in Fig. 3) remain near zero.

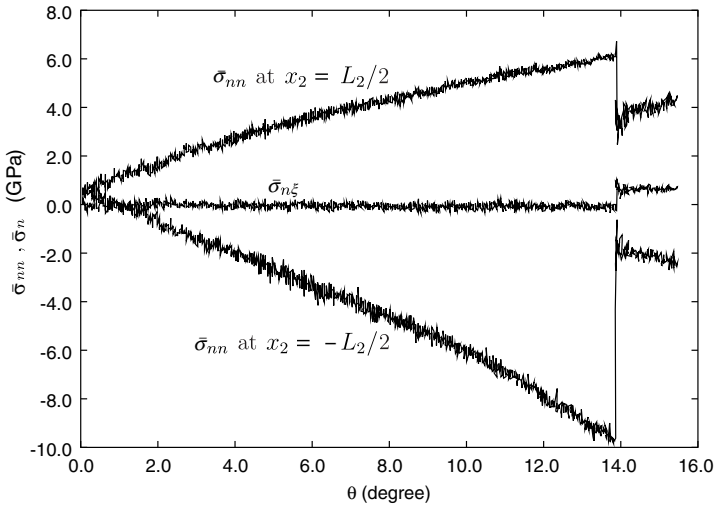

Fig. 3. Relation between stresses and bending angle for the crystal I with 24,282 atoms. Axial and shear stresses are calculated over the same volumes.

The corresponding stress–strain response at the compressive and tensile surfaces is shown in Fig. 4. Here, the strain is defined as $\sqrt{(\bar{s}_1/s_1)^2 - 1}$, where $\bar{s}_1$ is the width of the mid-section of the volume over which the stress is calculated in the current configuration and s_1 is its width prior to loading, see Fig. 1(c). Consistent with the tension-compression asymmetry of the Ercolessi and Adams (1994) potential, for a given magnitude strain, the magnitude of the compressive stress is greater than that of the tensile stress. This explains why nucleation occurs on the compressive side and not on the tensile side of the specimen. In Fig. 4, for crystal I, the outer fiber compressive strain at the onset of nucleation is 0.066.

The stress evolution for the largest specimen, crystal III, is shown in Fig. 5. Only time averaged values are plotted so no fluctuations appear. For this larger specimen, the stress at the tensile surface does not show a drop at dislocation nucleation. The outer fiber compressive strain at the onset of nucleation is 0.058 for crystal II and 0.065 for crystal III. Therefore, the local strains at the onset of dislocation nucleation are almost constant for the three crystals. Since the atomic stress at a free surface is not well defined, this suggests that a strain-based parameter may be used as a nucleation criterion.

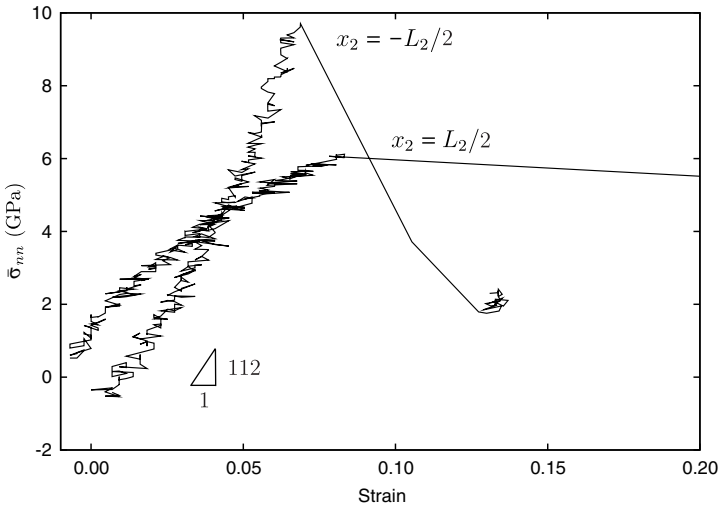

Fig. 4. Stress–strain curves for the upper and lower surfaces.

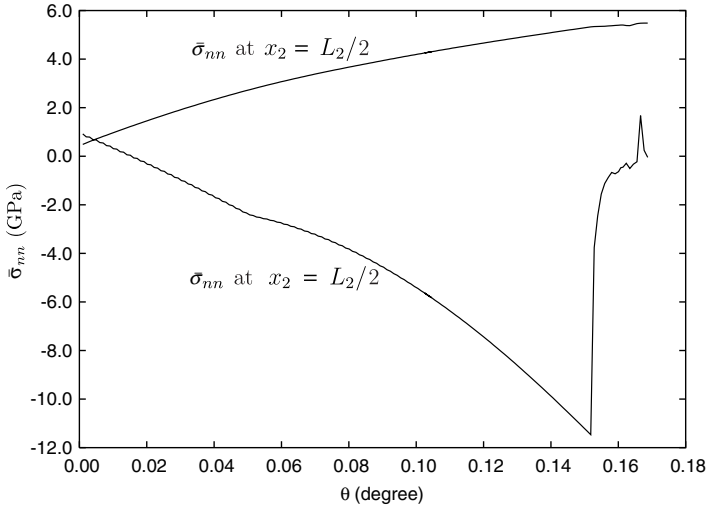

Fig. 5. Stresses as a function of bending angle for the model III with 102,542 atoms.

3.2. Structure of the nucleated dislocation

With increasing bending, each crystal deforms elastically until a dislocation nucleation event occurs. For all three size crystals, dislocations initiate from the lower surface simultaneously on (1 1 1) planes. To identify the nature of the initial dislocation structure, the relative displacements $s^{(\alpha\beta)}$ between atom α and its nearest neighbors is computed, where

$$s^{(\alpha\beta)} = |(\mathbf{x}^{(\beta)} - \mathbf{x}^{(\alpha)}) - (\mathbf{X}^{(\beta)} - \mathbf{X}^{(\alpha)})|, \quad \beta = 1, m \tag{5}$$

where m is the number of nearest neighbor atoms, $\mathbf{x}^{(\beta)}$ is the position vector in the current configuration of atom β and $\mathbf{X}^{(\beta)}$ is the position in the unloaded configuration of atom β. For the fcc crystallography analyzed, $m = 7$ for surface atoms and $m = 12$ for bulk atoms. The value of $s^{(\alpha\beta)}$ can be interpreted in a manner similar to a summation over all slipped neighbors (Zimmerman et al., 2001): the value of $s^{(\alpha\beta)}$ has a larger magnitude for dislocated inhomogeneous deformation near an atom and provides quantitative information about such deformation.

Fig. 6 shows the bent configuration[1] of crystal I, the smallest crystal, at the beginning of the bending moment drop, $\theta = 13.8°$. The region surrounding the defect and the surface atoms are shown since these atoms have higher potential energies. The process of dislocation loop nucleation is not yet complete, see Fig. 8. The magnitude of the slip quantity $s^{(\alpha\beta)}$ defined in Eq. (5) is in the range 0.1–0.2 nm at this stage of deformation. Since the Burgers vectors of a Shockey partial dislocation has a magnitude $b = 0.164$ nm, it is plausible that Shockey partials are being nucleated in Fig. 6.

In the $(\bar{1}\,\bar{1}\,1)$ plane, an ideal partial dislocation Burgers vector $[1\,1\,2]$ has components $0.288b$, $-0.166b$ and $0.942b$ along the x_1, x_2 and x_3 directions, respectively, while those for a $[2\,1\,1]$ partial in the $(1\,\bar{1}\,\bar{1})$ plane are $-0.288b$, $-0.833b$ and $0.477b$. By comparing the $s^{(\alpha\beta)}$ values with the ideal Burgers vector components, two slip vectors $[2\,\bar{1}\,1]$ and $[2\,1\,1]$ shown in Fig. 7 were found to give a close match. Because the slip vectors $[2\,\bar{1}\,1]$ and $[2\,1\,1]$ are in the $(\bar{1}\,\bar{1}\,1)$ and $(1\,\bar{1}\,\bar{1})$ planes, respectively, the half loops in Figs. 6 and 7 connected by the bowing-out free surface atoms must be slipping on such planes. This is consistent with independent slip plane calculations for the relaxed configuration shown in Fig. 8(b).

Fig. 7(b) shows atom positions at the free surface where dislocation nucleation occurs and Fig. 7(a) gives a projection view of all six (1 1 1) plane atoms that are originally located at the outermost lower surface shown in Fig. 7(b). A closer look at Fig. 7(a) and (b) reveals that the slip of an atom relative to its neighbors has two

[1] RASMOL (Sayle and Milner-White, 1995) is used for visualization.

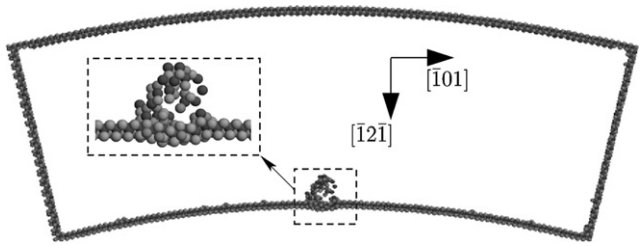

Fig. 6. Bending deformation and dislocation initiation for crystal I with 24,282 atoms. Atoms are colored (grayscale) according to their positions on the six (1 1 1) plane, i.e., atoms on the same plane are assigned one color. Only atoms with potential energies higher than −3.30 eV are plotted.

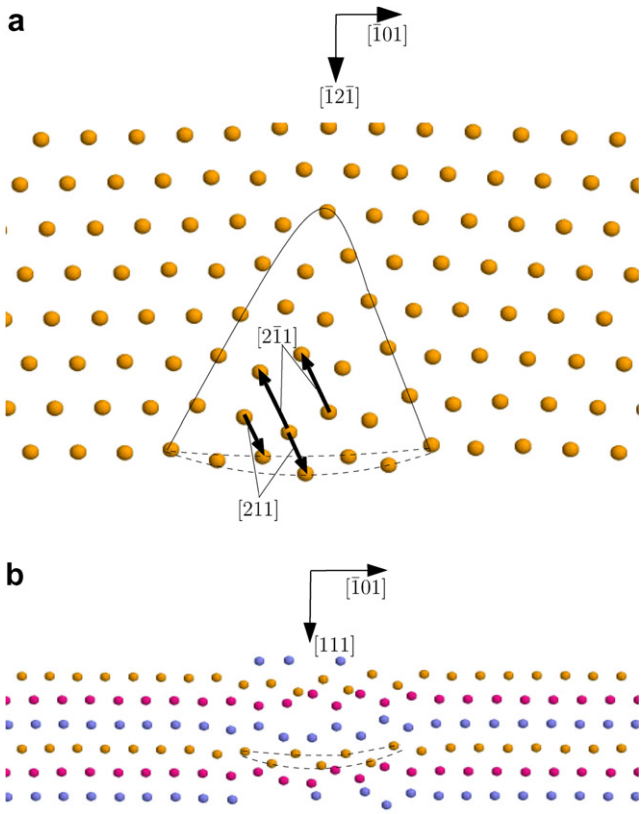

Fig. 7. Slip characters and a dislocation half loop. (a) Projection onto the (1 1 1) plane of atoms originally located on the same (1 1 1) plane; (b) projection onto the (1 $\bar{2}$ 1) plane of the outermost lower surface atoms on the six (1 1 1) planes. In (a), some of the easily identified slip vectors are shown. The atoms located on the dashed lines in (a) and (b) are the same.

main directional components: one in the [$\bar{2}$ 1 1] direction and the other in the [1 1 1] direction. This suggests that multiple slip must have been activated on the (1 $\bar{1}$ $\bar{1}$) and ($\bar{1}$ $\bar{1}$ 1) planes. Considering all possible slip directions of {1 1 0} and {2 1 1} in the above two slip planes and the directional components, the other slip directions are [1 1 2] on the ($\bar{1}$ $\bar{1}$ 1) plane on the right side of the dislocated region and [1 $\bar{1}$ 2] on the (1 $\bar{1}$ $\bar{1}$) plane on the left side of the dislocated region. The reason is that, on each of ($\bar{1}$ $\bar{1}$ 1) and (1 $\bar{1}$ $\bar{1}$) the two partial dislocation vectors, ($\bar{1}$ $\bar{1}$ 1)/[2 $\bar{1}$ 1]&[1 1 2] and (1 $\bar{1}$ $\bar{1}$)/[2 1 1]&[1 $\bar{1}$ 2], give a resultant Burgers vector that best matches the configurations shown in Fig. 7. The solid line half loop in Fig. 7 is drawn on the atoms that have close x_3 coordinates and this loop is also present in Fig. 6. The atoms lying on the dotted lines in Fig. 7(a) and (b) are the same atoms.

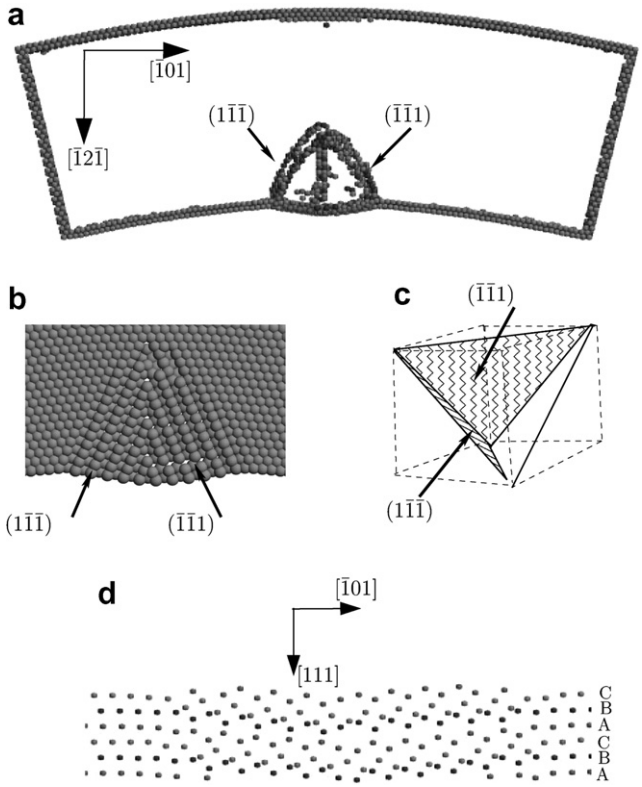

Fig. 8. Relaxed dislocation structure. (a) Details of the defected region; the atoms and their colors are chosen by the same criterion as in Fig. 6. (b) One layer atoms originally on the same (1 1 1) plane to indicate dislocated planes obtained by atomic positions. (c) Thompson's tetrahedron to show the crossing line between two neighboring {1 1 1} planes. (d) Outermost lower surface atoms projected on the indicated plane.

Because the nucleated dislocations are close together, the regions of large deformation associated with the dislocation cores overlap and there are relative displacements $s^{(\alpha\beta)}$ that do not correspond to any fcc slip direction. Calculations of $s^{(\alpha\beta)}$ show that none of the slip quantities give a vector for which the second component of the Burgers vector has the largest magnitude. This is evidence that the actually activated slips cannot be of the type $[1\,\bar{2}\,\bar{1}]$ on the $(\bar{1}\,\bar{1}\,1)$ plane nor $[\bar{1}\,\bar{2}\,1]$ on the $(1\,\bar{1}\,\bar{1})$ plane. Atomic configurations at an earlier time are shown subsequently in Section 4 and there is no change from Figs. 2 and 3 in the nature of dislocations nucleated.

In summary, the dislocations nucleated are of the nature $(\bar{1}\,\bar{1}\,1)/[2\,\bar{1}\,1]\&1\,1\,2]$ and $(1\,\bar{1}\,\bar{1})/[2\,1\,1]\&[1\,\bar{1}\,2]$. In case the two partials on each of the slip planes were equally large, they react to form [1 0 1] dislocations that are kinematically compatible with bending.

Following dislocation nucleation, the molecular dynamics calculation was continued for 5000 time steps, keeping the imposed rotation θ fixed. The relaxed equilibrium dislocation structures are shown in Fig. 8. Based on the fact that any three points in space that are not located on the same line comprise a plane, calculation of the plane normal vector is carried out by arbitrarily selecting three atoms lying in the parallel planes indicated by arrows in Fig. 8. The result is shown in Fig. 8(b), where one can identify several parallel $(\bar{1}\,\bar{1}\,1)$ and $(1\,\bar{1}\,\bar{1})$ planes in the dislocated region. The magnitude of the slip measure $s^{(\alpha\beta)}$ is as large as 0.29 nm at this stage. However, dislocation reactions that occurred during the relaxation process make it difficult to identify the Burgers vector of individual dislocations. Nevertheless, several salient features in the dislocation structure can be seen. The half loops in Fig. 8(a) are comprised of sub-loops: on each slip plane two slip directions are activated, each of which makes a sub-loop. These loops evolve and expand in size. This dislocation nucleation behavior contrasts with that found by Li et al. (2002) for spherical indentation of Al (using the same

Ercolessi–Adams potential), where the dislocation is reported to be initiated from one {1 1 1} plane and then spread to adjacent {1 1 1} planes. On the other hand, it does share features seen by Hess et al. (2005) in the nucleation of a dislocation from a crack tip.

The magnitude of the slip vectors of the dislocation loops varies depending on position, with the largest values near the free surface and gradually decreasing in magnitude towards the top crossing points of the intersecting loops. In Fig. 8(a), there are rod-like [1 0 1]-type dislocation lines which are the lines crossed by two {1 1 1} glide planes that can be identified in the Thompson tetrahedron, Fig. 8(c). In Fig. 8(d), some atoms pass out of the periodic 'box' and then re-enter from the opposite side. This is due to the periodic boundary condition along the [1 1 1] direction and the fact that the dislocation vectors have a component in the [1 1 1] direction.

For the largest crystal considered, crystal III, the dislocation structure at the onset of nucleation is shown in Fig. 9. The slip vectors between one atom and its neighbors in the defected regions have similar directional characteristics, but have smaller lengths (<0.15 nm) than those in Figs. 6–8. The glide directions of the partial dislocations activated are believed to be the same as in Figs. 6–8. One common feature of the dislocation structures is that they are formed by activating two slip planes in two glide directions. Such dislocation structures contrast with the classical extended structures with a bend where glide occurs from one slip plane to another (cf. Hirth, 2000), but have also been observed during dislocation nucleation from a crack tip (Hess et al., 2005). It is also noted that the surface dislocations does not form surface steps, but 'swell out' instead as convex continuous smooth curvatures. However, there are several significant differences between the behavior of crystal III relative to crystal I: (1) the dislocated regions appear at two sites symmetrically located from the center of the specimen instead of concentrating at one center site, (2) the dislocations at the two sites occur

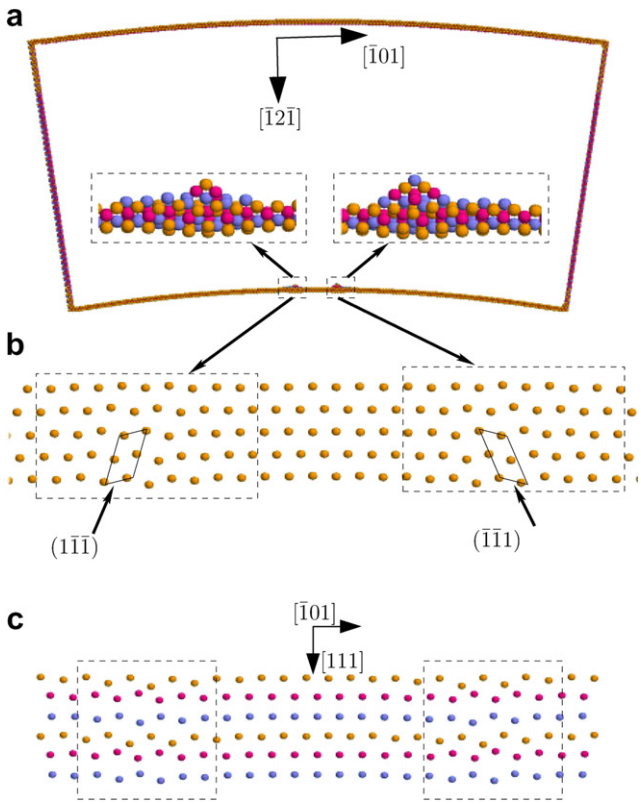

Fig. 9. Bending deformation at dislocation initiation for the model III of 102,542 atoms. (a) Dislocations are developed at two sites symmetrically distributed from the center line, (b) atoms originally located on one (1 1 1) plane to show the glide planes and (c) outermost lower surface atoms projected on the plane indicated. The colors have the same meaning as in Fig. 7. Defected regions are enclosed by dashed lines, smaller in size and more stable upon relaxation than the previous model.

on different slip plane as shown in Fig. 9(b), and (3) sufficient relaxation in the same way as mentioned above results in only slight size change of the defected regions. The results for the intermediate size crystal, crystal II, are similar to those for crystal III and are not shown.

4. Dislocation nucleation criteria

4.1. Critical resolved shear stress

For fcc metals such as Al, gross plastic deformation on a slip plane is, to a good degree of approximation, associated with the shear stress resolved on that slip plane reaching a critical value. The association between the slip plane resolved shear stress and plastic deformation also holds at the dislocation level through the Peach–Koehler configurational force work conjugate to dislocation motion. Here, we explore the extent to which a critical values of the resolved shear stress characterizes the onset of dislocation nucleation in our calculations. The resolved shear stress is calculated as $\tau = \sigma_{ij} m_i t_j$, where σ_{ij} is obtained from Eq. (2) and m_i and t_j are the components of the unit normal and tangent vectors to the crystallographic plane. The resolved shear stress at nucleation, τ_{nuc}, is calculated in the volume element near the compressive surface in which dislocation nucleation first occurs at the stress peak (see Figs. 6–9).

For crystal I, the value of τ_{nuc} is 2.46 GPa for the slip system $(\bar{1}\,\bar{1}\,1)/[2\,\bar{1}\,1]$, 1.87 GPa for the slip system $(\bar{1}\,\bar{1}\,1)/[1\,1\,2]$ and 4.33 GPa for $(\bar{1}\,\bar{1}\,1)/[\bar{1}\,2\,1]$. For the $(1\,\bar{1}\,\bar{1})/[2\,1\,1]$ slip system $\tau_{\text{nuc}} = 1.87$ GPa, for the $(1\,\bar{1}\,\bar{1})/[1\,\bar{1}\,2]$ slip system $\tau_{\text{nuc}} = 2.46$ GPa, and for $(1\,\bar{1}\,\bar{1})/[\bar{1}\,2\,1]$, $\tau_{\text{nuc}} = 4.33$ GPa. However, no dislocation nucleation occurs on the $(1\,\bar{1}\,\bar{1})/[\bar{1}\,\bar{2}\,1]$ slip system. Dislocation nucleation occurred on the slip systems $(\bar{1}\,\bar{1}\,1)/[2\,\bar{1}\,1]$, $(\bar{1}\,\bar{1}\,1)/[1\,1\,2]$, $(1\,\bar{1}\,\bar{1})/[2\,1\,1]$ and $(1\,\bar{1}\,\bar{1})/[1\,\bar{1}\,2]$ with resolved shear stresses of 1.87 or 2.46 GPa.

For crystal III, for the $(\bar{1}\,\bar{1}\,1)$ plane dislocation, the values of τ_{nuc} on the systems values of $(\bar{1}\,\bar{1}\,1)/[2\,\bar{1}\,1]$, $(\bar{1}\,\bar{1}\,1)/[1\,1\,2]$ and $(\bar{1}\,\bar{1}\,1)/[\bar{1}\,2\,1]$ are 3.69 GPa, 1.75 GPa and 5.44 GPa, respectively. For the $(1\,\bar{1}\,\bar{1})$ plane, the directions $[2\,1\,1]$, $[1\,\bar{1}\,2]$ and $[\bar{1}\,\bar{2}\,1]$ are subjected to resolved shear stresses of $\tau_{\text{nuc}} = 2.33$ GPa, 2.88 GPa and 5.21 GPa, respectively. Again, dislocation nucleation does not occur on the system with the largest value of resolved shear stress. Dislocation nucleation occurred on the slip systems $(\bar{1}\,\bar{1}\,1)/[2\,\bar{1}\,1]$, $(\bar{1}\,\bar{1}\,1)/[1\,1\,2]$, $(1\,\bar{1}\,\bar{1})/[2\,1\,1]$ and $(1\,\bar{1}\,\bar{1})/[1\,\bar{1}\,2]$ with resolved shear stresses $\tau_{\text{nuc}} = 3.69$ GPa, 1.75 GPa, 2.33 GPa and 2.88 GPa, respectively.

In all calculations here, the slip systems with the largest resolved shear stress were not activated. In addition, the values of τ at which dislocation nucleation occurs are almost one order in magnitude smaller than those for nucleation in the bulk material (Shenoy et al., 2000). This is consistent with weaker bonding at a free surface than in the interior. However, it should also be noted that stress as defined in (2) is essentially a bulk quantity. The nano-indentation studies of Zimmerman et al. (2001) and Miller and Acharya (2004) also showed that a critical resolved shear stress criterion for dislocation nucleation did not hold, while in those studies dislocation nucleation took place in the interior.

4.1.1. Elastic stability criterion

In continuum elasticity, the onset of a material instability is associated with the Hadamard condition of loss of positive definiteness of the matrix Λ_{jl} defined by

$$\Lambda_{jl} = C_{ijkl} v_i v_k + \sigma_{jl} \tag{6}$$

for any unit vector v_i (cf. Hill, 1962; Rice, 1976). Here, the current and reference configurations are assumed to coincide and C_{ijkl} are the components of the instantaneous elastic moduli. For sufficiently small deformations, Λ_{jl} is positive definite. If a state is subsequently attained where $\det \Lambda_{jl} = 0$ loss of stability occurs in the sense that can be interpreted both as localization into a deformation band and as a body wave with zero wave speed (Hill, 1962; Rice, 1976).

Van Vliet et al. (2003) have explored the use of this stability criterion as a criterion for homogeneous dislocation nucleation in Al during spherical indentation. When $\det \Lambda_{jl} = 0$, the direction v_i is the normal to the localization plane and the equation $\Lambda_{jl} k_l = 0$ is solved to obtain the deformation direction. They found that homogeneous dislocation nucleation did occur at the lowest loading level for which $\det \Lambda_{jl} = 0$. Furthermore,

the corresponding orientation v_i agreed well with the glide plane normal of the nucleated dislocation. However, the deformation direction given by the eigenvector differed from the Burgers vector of the nucleated dislocation by $\sim 12°$.

We have attempted to apply this criterion to the onset of dislocation nucleation from a free surface in our calculations. It was found that $\det \Lambda_{jl} = 0$ occurred in the undeformed state. This is most likely a consequence of the definition of stress in (2) and the moduli C_{ijkl} being appropriate bulk definitions but not surface definitions; indeed, the restriction to the bulk has been noted already by Zhu et al. (2004).

4.1.2. Stress-gradient based criterion

Using nonlinear elasticity, Acharya (2003) derived driving forces for dislocation velocity and nucleation rates. The dislocation nucleation criterion that emerged is a nonlocal one; i.e. the onset of nucleation depends on the value of field quantities throughout the body, not just at the location where dislocation nucleation takes place. Miller and Acharya (2004) subsequently developed a simplified criterion that was explored here. The onset of dislocation nucleation occurs when

$$N \geqslant N_{\text{crit}} \tag{7}$$

where

$$N = \left| t_i e_{rjk} \frac{\partial \sigma_{ik}}{\partial x_j} l_r \right| \tag{8}$$

Here, t_i are the components of a unit vector parallel to the Burgers vector, l_r are the components of a unit vector tangent to the dislocation line, e_{rjk} is the permutation tensor, and $||$ denotes absolute value. From two-dimensional molecular dynamics analyses but with a fully three-dimensional underlying crystal lattice, Miller and Acharya (2004) reported several successful predictions of bulk dislocation nucleation using the stress-gradient criterion (7) and (8). The stress-gradient based criterion was able to reproduce atomistic dislocation nucleation results in cases where a critical resolved shear stress criterion failed.

Here, we explore using this stress-gradient criterion for dislocation nucleation from a free surface. Because our molecular dynamics calculations are three-dimensional, the dislocation line direction can lie anywhere in the slip plane and maximization of N involves an additional degree of freedom as compared with the two-dimensional implementation. In addition, the proximity of the free surface presents difficulties in defining an accurate atomic stress. To evaluate N, the orientation of l_r in the slip plane was varied at each atom from 0° to 360° in 1° increments. For each atom, N was calculated for all possible slip directions in the slip planes $(\bar{1}\,\bar{1}\,1)$ and $(1\,\bar{1}\,\bar{1})$. To obtain stress gradients $\partial\sigma_{ik}/\partial x_j$, linear, four node tetrahedral elements and their shape functions were used to interpolate stresses between atoms and the stress gradients for each element were computed from the interpolation function. For atoms shared by adjacent elements, the value of the stress gradient at that atom is the average over the shared elements.

If N_{crit} is taken to be the maximum N over all atoms there will be just one atom that satisfies Eq. (7). For generation of a dislocation loop we require N_{crit} in Eq. (7) to be smaller than the maximum N over all atoms involved, so as to permit a dislocation loop to be formed. Fig. 10 shows the predictions for crystal I. Here, atoms are colored by the maximum value of N at an atom, with red corresponding to the higher values of N. The maximum values of N for crystals I, II and III are 0.28, 0.36 and 0.37 eV Å^{-4} (=0.45, 0.58 and 0.59×10^{-9} N nm^{-3}), respectively. Fig. 10(a) and (b) corresponds to the C-layer and B-layer atomic planes in Figs. 7 and 8, respectively. The atomic configurations represents an earlier time sequence (the same θ but smaller relaxation time steps) than those of Figs. 6 and 7 and the largest relative slips s reach roughly 1.1 nm smaller than a partial Burgers length, but have all the characteristics elaborated in Section 3.1, so there is no change in the nature of dislocations. In Fig. 10(a) and (b), two dislocation loops are predicted to occur, of the type $(\bar{1}\,\bar{1}\,1)/[1\,\bar{2}\,\bar{1}]$ and $(1\,\bar{1}\,\bar{1})/[\bar{1}\,\bar{2}\,1]$, but these were not actually found in the MD simulations. Shown in Fig. 10(b) are dislocations nucleated on one neighboring (1 1 1) plane. The stress-gradient concept correctly predicts two dislocations of $(\bar{1}\,\bar{1}\,1)$ [1 1 2] and $(1\,\bar{1}\,\bar{1})$ $[1\,\bar{1}\,2]$, while give a dislocation of the type $(1\,\bar{1}\,\bar{1})$ $[\bar{1}\,\bar{2}\,1]$ at the same time, which is not existing in the MD simulation. Besides, this criterion does not predict simultaneous nucleation at all (1 1 1) planes because the $N_{m,l}$ values for A-atom layers in Figs. 7 and 8 are almost one

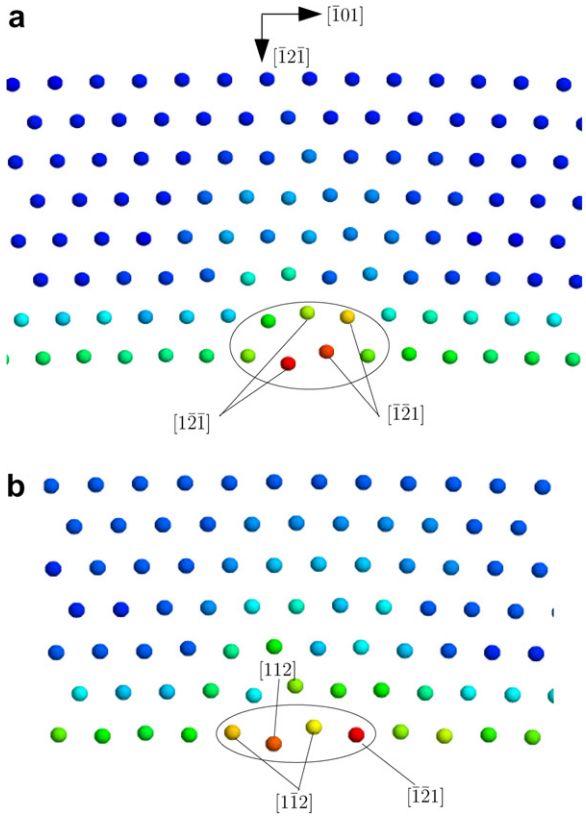

Fig. 10. Dislocation nucleation predicted by the stress-gradient based criterion for two neighboring (1 1 1) planes; (a) the top layer of yellow atoms and (b) the next, red layer in Fig. 7.

order of magnitude smaller than those shown in Fig. 10(a) and (b). The discrepancy may be due to approximations made in the derivation of (8) (Acharya, 2003; Miller, 2002).

5. Conclusions

Molecular dynamics calculations of aluminum single crystals subject to a prescribed rotation were carried out. Regarding the nucleation of dislocations from the free surfaces, the following conclusions were obtained:

- The initial dislocation structure consist of half loops that are nucleated simultaneously on {1 1 1} planes.
- The critical resolved shear stress at nucleation is much lower than reported for dislocation nucleation in the bulk using the same embedded atom potential.
- The local strains at the onset of dislocation nucleation show little model size dependency.
- Dislocation nucleation is not well-represented by a critical value of the resolved shear stress.
- The onset of dislocation nucleation is reasonably well-represented by the stress-gradient criterion proposed by Acharya (2003) and Miller and Acharya (2004).

Acknowledgments

It is a pleasure to thank David L. Olmsted, Vijay Shastry, Sharvan Kumar and Vivek B. Shenoy for many fruitful discussions. We are also pleased to acknowledge support from the MRSEC Program of the National Science Foundation under award DMR-0520651 to Brown University. Additional funding to YFL was provided by National Institute for Materials Science, Tsukuba City, Japan.

References

Acharya, A., 2003. Driving forces and boundary conditions in continuum dislocation mechanics. Proceedings of the Royal Society of London, Series A—Mathematical Physical and Engineering Sciences 459 (2034), 1343–1363.

Allen, M., Tildesley, D., 1987. Computer Simulation of Liquids. Oxford University Press, New York, pp. 46–49.

Beltz, G.E., Rice, J.R., 1992. Dislocation nucleation at metal ceramic interfaces. Acta Metallurgical et Materialia 40, S321–S331.

Benzerga, A.A., Bréchet, Y., Needleman, A., Van der Giessen, E., 2004. Incorporating three-dimensional mechanisms into two-dimensional dislocation dynamics. Modeling and Simulation in Materials Science and Engineering 12 (1), 159–196.

Brochard, S., Beauchamp, P., Grilhé, J., 2001. Simulation of dislocation nucleation from atomic size surface steps and grooves. Materials Science and Engineering A 309–310, 456–462.

Christiansen, J., Morgenstern, K., Schiøtz, Jacobsen, K.W., Braun, K.-F., Rieder, K.-H., Lægsgaard, E., Besebbacger, F., 2002. Atomic-scale structure of dislocations revealed by scanning tunneling microscopy and molecular dynamics. Physical Review Letters 88 (20).

Daw, M.S., Baskes, M.I., 1984. Embedded-atom method – derivation and application to impurities, surfaces and other defects in metals. Physical Review B 29 (12), 6443–6453.

Ercolessi, F., Adams, J.B., 1994. Interatomic potentials from 1st-principles calculations – the force-matching method. Europhysics Letters 26 (8), 583–588.

Gao, Y.F., Yu, H.H., Kim, K.S., submitted for publication. Microplasticity of surface steps under adhesive contact. Part II. Multiple-dislocation mediated surface hardening.

Hess, B., Thijsse, B.J., Van der Giessen, E., 2005. Molecular dynamics study of dislocation nucleation from a crack tip. Physical Review B 71, 054111.

Hill, R., 1962. Acceleration waves in solids. Journal of the Mechanics and Physics of Solids 10, 1–16.

Hirth, J.P., 2000. Some current topics in dislocation theory. Acta Materialia 48 (1), 93–104.

Hoover, W.G., 1985. Canonical dynamics: equilibrium phase-space distributions. Physical Review A 31 (3), 1695–1697.

Kelchner, C.L., Plimpton, S.L., Hamilton, J.C., 1998. Dislocation nucleation and defect structure during surface indentation. Physical Review B 58 (17), 11085–11088.

Kubin, L., Canova, G., 1992. The modeling of dislocation patterns. Scripta Metallurgica et Materialia 27 (8), 957–962.

Li, J., Vliet, K.J.V., Zhu, T., Yip, S., Suresh, S., 2002. Atomistic mechanisms governing elastic limit and incipient plasticity in crystals. Nature 418, 307–310.

Miller, R., 2002. Private communication.

Miller, R., Acharya, A., 2004. A stress-gradient based criterion for dislocation nucleation in crystals. Journal of the Mechanics and Physics of Solids 52 (7), 1507–1525.

Nose, S., 1984. A unified formulation of the constant temperature molecular dynamics methods. The Journal of Chemical Physics 81 (1), 511–519.

Rice, J.R., 1976. The localization of plastic deformation. In: Koiter, W.T. (Ed.), Theoretical and Applied Mechanics. North-Holland, pp. 207–219.

Rice, J.R., Thomson, R., 1974. Ductile versus brittle behavior of crystals. Philosophical Magazine 29 (1), 73–97.

Sayle, R., Milner-White, E.J., 1995. RASMOL: biomolecular graphics for all. Trends in Biochemical Sciences 20 (9), 374–376.

Shan, D., Yuan, L., Guo, B., 2005. Multiscale simulation of surface step effects on nanoindentation. Materials Science and Engineering A 412, 264–270.

Shenoy, V.B., Phillips, R., Tadmor, E.B., 2000. Nucleation of dislocations beneath a plane strain indenter. Journal of the Mechanics and Physics of Solids 48 (4), 649–673.

Van der Giessen, E., Needleman, A., 1995. Discrete dislocation plasticity: a simple planar model. Modeling and Simulation in Materials Science and Engineering 3 (5), 689–735.

Van Vliet, K.J., Li, J., Zhu, T., Yip, S., Suresh, S., 2003. Quantifying the early stages of plasticity through nanoscale experiments and simulations. Physical Review B 67 (10).

Weingarten, N.S., Selinger, R.L.B., 2006. Size effects and dislocation patterning in two-dimensional bending. Preprint cond-mat/0606789.

Xu, G., Argon, A.S., Ortiz, M., 1995. Nucleation of dislocations from crack tips under mixed-mode loading – implications for brittle against ductile behavior of crystals. Philosophical Magazine A – Physics of Condensed Matter Structure Defects and Mechanical Properties 72 (2), 415–451.

Yu, H.H., Shrotriya, P., Gao, Y.F., Kim, K.S., accepted for publication. Microplasticity of surface steps under adhesive contact. Part I. Surface yielding controlled by single-dislocation nucleation. Journal of the Mechanics and Physics of Solids.

Zbib, H., Rhee, M., Hirth, 1998. On plastic deformation and the dynamics of 3D dislocations. International Journal of Mechanical Sciences 40 (2–3), 113–127.

Zhu, T., Li, J., Van Vliet, K.J., Ogata, S., Yip, S., Suresh, S., 2004. Predictive modeling of nanoindentation-induced homogeneous dislocation nucleation in copper. Journal of the Mechanics and Physics of Solids 52 (3), 691–724.

Zimmerman, J.A., Kelchner, C.L., Klein, P.A., Hamilton, J.C., Foiles, S.M., 2001. Surface step effects on nanoindentation. Physical Review Letters 87 (16).